JOURNAL OF AIRCRAFT
Vol. 46, No. 2, March–April 2009

Numerical and Experimental Validation of Three-Dimensional Shock Control Bumps

Benedikt König,* Martin Pätzold,† Thorsten Lutz,‡ and Ewald Krämer§
Universität Stuttgart, 70550 Stuttgart, Germany
Henning Rosemann¶ and Kai Richter¶
DLR, German Aerospace Center, 37073 Göttingen, Germany
and
Heiko Uhlemann**
German-Dutch Wind Tunnels, 37073 Göttingen, Germany

DOI: 10.2514/1.41441

Numerical and experimental studies have been performed to show the potential for drag reductions of an array of discrete three-dimensional shock control bumps. The bump contour investigated was specifically designed by means of computational-fluid-dynamics-based numerical optimization for wind-tunnel testing on a modern transonic airfoil. The experimental investigations focused on turbulent flow at a Reynolds number of 5 million and were carried out at the Transonic Wind Tunnel Göttingen. Drag reductions of around 10% in the drag-rise region were found in the experiment even though the results were influenced by wind-tunnel interference effects. A detailed numerical study of the wind-tunnel environment reproduced the influence of the wind-tunnel walls on the bump performance and gave good agreement to the experimental results.

Nomenclature

C_d, C_l, C_p	=	coefficients of drag, lift, and pressure
c	=	airfoil chord length
dY	=	spanwise position of the wake rake
h_{scb}	=	bump crest height
M	=	Mach number
p_{exit}	=	static pressure at the test section exit
p_0	=	total pressure
Re	=	Reynolds number
T_0	=	total temperature
x, y, z	=	Cartesian coordinate directions
x_{pos}	=	streamwise position of the bump crest
x_{tr}	=	transition location
y^+	=	dimensionless wall distance
α	=	angle of attack
δ^*	=	displacement thickness

I. Introduction

INCREASING the aerodynamic efficiency is one of the main design issues for modern commercial transport aircraft. Drag reduction thereby not only influences the operating costs for the airlines but also has a direct impact on fuel consumption and environmental pollution. Schneider [1] points out that, for typical current long-range aircraft, a drag reduction of 1% will result in fuel savings of about 400,000 liters per year, per aircraft. This corresponds to about 5000 kg of noxious emissions. Today's long-range transport aircraft typically cruise within the transonic speed regime to maximize the operational range as well as cruise speed. The upper limit in cruise speed is usually set by shock waves, terminating areas of supersonic flow, and the associated drag rise at off-design conditions. Shock control is therefore one important means of extending the operational range and of improving the off-design characteristics.

A thorough study of different methods for shock and shock/boundary-layer interaction control was performed in the European research project EUROSHOCK II [2]. Detailed numerical and experimental investigations on shock control mechanisms, including discrete suction, ventilation, and local contour modifications, were presented by Knauer [3] and Birkemeyer [4]. One of the conclusions drawn from EUROSHOCK II was that the so-called shock control bump [5] (SCB) was the most effective control scheme studied therein. Investigations by Sommerer et al. [6,7] showed that wave drag reductions of up to 75% were possible through the application of an SCB on two-dimensional airfoil sections. Kutzbach et al. [8] investigated the influence of the three-dimensional boundary layers of swept wings on the effectiveness of SCBs on infinite swept wings. Rosemann et al. [9] applied and wind-tunnel tested a single bump on the outboard wing of a transonic wing–body configuration. All these bumps studied hitherto were two-dimensional in the sense that there were no, or only negligible, effects from spanwise flanks due to a finite bump width. In contrast to that, bumps with significant effects due to their lateral flanks, that is, with a small width/depth ratio, will in this work be denoted as three-dimensional shock control bumps (3D-SCBs).

Experimental results of control using three-dimensional shock wave boundary-layer interaction with spanwise discrete arrays of slots, grooves, and bumps were presented by Holden and Babinsky [10] and by Babinsky and Ogawa [11]. It was shown that these arrays of discrete devices may offer comparable potential as two-dimensional devices. Recent work by Rein et al. [12] demonstrated the wave drag reducing three-dimensional oblique shock structures that were achievable by aerospikes placed above the airfoil surface. Three-dimensional effects of finite shock control bumps in particular were numerically studied by Qin et al. [13] and Pätzold et al. [14,15], the latter with an emphasis on the application on swept wings. In [16], Ogawa et al. showed experimental measurements of three-dimensional bumps mounted on a wind-tunnel wall and numerical

Presented as Paper 4001 at the 4th Flow Control Conference, Seattle, WA, 23–26 June 2008; received 7 October 2008; revision received 30 January 2009; accepted for publication 31 January 2009.

*Research Engineer, Institute of Aerodynamics and Gasdynamics. AIAA Member
†Research Engineer, Institute of Aerodynamics and Gasdynamics.
‡Senior Researcher, Institute of Aerodynamics and Gasdynamics
§Head of Institute of Aerodynamics and Gasdynamics.
¶Senior Researcher, Institute of Aerodynamics and Flow Technology, Bunsenstrasse 10.
**Research Engineer, Bunsenstrasse 10.

studies of the same bumps on a transonic airfoil with comparable flow conditions upstream of the shock. Again, the influence of the finite bumps over the whole span was shown, together with some distinct three-dimensional effects between the bumps.

However, until recently, no experimental verification of the numerically predicted drag reductions by 3D-SCBs on an airfoil have been performed. Such an experiment has finally been conducted at the Transonic Wind Tunnel Göttingen [17] (TWG) for a transonic airfoil equipped with an array of specially designed three-dimensional shock control bumps. The results obtained from the experiments have shown promising drag reductions of the expected size but there have been discrepancies between the findings and the numerical simulations conducted beforehand. Extensive numerical simulations, including the modeling of the wind-tunnel environment, have revealed that wind-tunnel wall interferences present in the experiment have confounded the results [18]. Accounting for the wind-tunnel walls in the computational fluid dynamics (CFD) simulations provided the ability to reproduce the relevant interference effects in the wind tunnel and thereby improved the agreement between experimental and numerical results. This paper presents the numerical and experimental setup used for the investigations on three-dimensional shock control bumps. A short introduction into the flow physical effects related to the 3D-SCB is given before experimental results and a detailed numerical analysis thereof is presented.

II. Experimental Arrangement

A. Transonic Wind Tunnel Göttingen

The Transonic Wind Tunnel Göttingen, belonging to the German-Dutch Wind Tunnels (DNW), is a continuous, pressurizable wind tunnel with three exchangeable test sections for subsonic, transonic, and supersonic speeds. Possible inflow Mach numbers range from $M = 0.3$ to 2.2 and the freestream Reynolds number can be varied between $Re = 4 \times 10^6$ m^{-1} and $Re = 18 \times 10^6$ m^{-1} by changing the stagnation pressure. The experiments presented herein were carried out in the 1×1 m adaptive walls test section [17]. This test section offers two-dimensional adaptation of the upper and lower test section walls to streamlines of the internal flow, based on the Cauchy integral formula by Amecke [19]. The upper flexible wall is equipped with 22 jacks to adjust the wall shape and the bottom wall uses 20 jacks for adaptation. Besides the wall adaptation during the tests, no further wind-tunnel corrections were applied to the results. The test was carried out at a Mach number of $M = 0.79$ and a Reynolds number of $Re = 5.0 \times 10^6$, based on the model's chord length of 40 cm. Because of the rather high Mach number for a closed test section, a certain degree of wall interferences was to be expected.

The vertical and horizontal test section walls were equipped with several rows of pressure orifices to gather static wall pressure along the test section. A stationary wake rake with 128 pitot tubes for total pressure measurements and eight static pressure taps was available for drag evaluation. The height of the wake rake was 0.5 m and it was located at a distance of 1.5 chord lengths behind the model. The wind tunnel was also calibrated for the application of the pressure sensitive paint (PSP) technology of the German Aerospace Center (DLR) [20]. For the measurements presented here, no balance for direct measurement of the aerodynamic forces was available. Sobieczky [21] states an accuracy for the TWG of $\Delta M \approx 0.001$, $\Delta\alpha \approx 0.02$ deg, and $\Delta C_p \approx 0.002$. The overall turbulence level is given as $Tu < 0.35\%$.

B. Model

A modern transonic airfoil was used as datum airfoil for the measurements. The steel airfoil model had a chord length of $c = 0.4$ m, a span of 1.0 m, and a maximum thickness of 8.18%. It was equipped with 126 pressure taps in three sections on the upper surface with 42 pressure taps in each section. The lower surface had an additional 28 pressure taps to determine aerodynamic lift by surface pressure integration. The model was mounted horizontally in the test section with the model's leading edge located at a downstream position of $x_{le} = 1.97$ m from the test section entry. The mounting mechanism allowed for a traversing of the model of 0.1 chord lengths (i.e., 4 cm) relative to the wake rake. This was necessary for measurements of the spanwise varying local drag with the stationary mounted wake rake for the airfoil with SCBs.

Eleven shock control bumps with a base area of 8×4 cm each were cemented onto the airfoil models suction side. The spanwise spacing was 4 cm between two consecutive bumps. The shape of the bumps was specially designed for the datum airfoil and the inflow conditions tested. Special care was taken to ensure that the bump contour, manufactured from glass fiber composite, exactly reproduced the numerically designed shape. A minimal material thickness of one layer of glass fiber cloth was realized at the fringe of the bumps to achieve smooth transitions without curbs from the bump to the airfoil surface. The bump's shape design and the optimization process will be described further in Sec. IV.A together with the design parameters and constraints. The placement of the bumps on the airfoil surface covered several of the pressure taps and thus made the automatic lift calculation by pressure integration in the experiment impossible. Hence, no information on the lift was available during the measurements. Figure 1 shows a photograph of the model with SCBs and the wake rake in the test section in downstream direction.

Transition strips were applied to the airfoil model at $x_{tr}/c = 0.1$ on the pressure and suction side to enforce transition. Calculations with the multi-element design and analysis tool MSES [22] were used to estimate the minimum height of the transition strip's roughness elements to ensure bypass transition at the flow conditions tested. Trip disks with a height of 0.127 mm, a diameter of 1.0 mm, and a spanwise spacing of 2.54 mm were selected.

The pressure sensors on the airfoil model surface did not provide the spatial resolution necessary for detailed visualization of the expected flow characteristics of the shock control bumps. Moreover, the pressure sensors in the most interesting region of the shock were partly covered by the additionally fitted bumps and were therefore not available for measurements at the bump positions. Thus, the PSP technology of DLR [20] was applied for some of the measurements to gather high-resolution surface pressure distributions.

C. Test Program

The test program for the SCB measurements comprised a limited number of the aforementioned PSP measurements and a set of polars for a range of inflow Mach numbers with wake drag measurements only. However, a tight time schedule led to the cancellation of the tests at different Mach numbers. The reduced and finally realized test program is summarized in Table 1. The Reynolds number is based on the chord length of the airfoil model and α indicates the range of the angles of attack, with $\Delta\alpha$ being the angular resolution of the measured polars. The translational displacement dY denotes the traversal position of the airfoil model for wake measurements at varying spanwise positions. The position $dY = 0$ mm corresponds

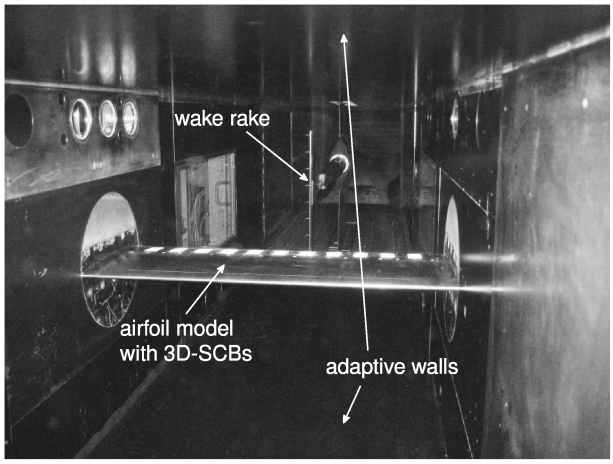

Fig. 1 Model with 3D-SCBs in the adaptive walls test section of the Transonic Wind Tunnel Göttingen (TWG).

Table 1 Flow conditions tested at the TWG

M	Re	α, deg	$\Delta\alpha$, deg	dY, mm	SCB	PSP
0.790	5×10^6	1.0–4.5	0.1,. . .,0.25	0; 40	On	On
0.790	5×10^6	1.5–3.5	0.1,. . .,0.25	0; 10; 20; 30; 40	On	Off
0.790	5×10^6	1.5–3.5	0.1,. . .,0.25	0	Off	Off

to the center behind the innermost SCB whereas $dY = 40$ mm is the position midway between two SCBs.

III. Computational Setup

A. Numerical Method

1. *Reynolds-Averaged Navier–Stokes Analysis Tool FLOWer*

The CFD simulations presented in this work were performed using the FLOWer code [23] developed by DLR, German universities, and industry. FLOWer is a well-established code of nominally second-order accuracy that solves the compressible, two- or three-dimensional Reynolds-averaged Navier-Stokes (RANS) equations on block-structured finite volume grids. The convective fluxes of the main equations are discretized in space by the common Jameson–Schmidt–Turkel central scheme with a blend of second- and fourth-order artificial damping terms. Matrix dissipation according to Swanson and Turkel [24] is available as well and was applied to the simulations of the wind-tunnel environment presented later. Time integration toward the steady state of the main equations was accomplished by an explicit five-stage Runge–Kutta scheme with local time stepping, and convergence was accelerated by means of implicit residual smoothing and a multigrid method. The computations shown herein were accomplished by closing the RANS equations using Menter's two-equation shear stress transport model. The turbulence model's influence on the results was investigated by alternatively applying the SALSA variant of the Spalart–Allmaras one-equation turbulence model, the linear explicit algebraic stress model, and the seven-equation full Reynolds stress model according to Wilcox [25]. The capability of the FLOWer code to capture shock-induced separations was previously validated against the well-known RAE-2822 airfoil [15].

2. *Optimization Environment*

The design of the three-dimensional shock control bumps for wind-tunnel testing was performed using the Parallel Optimization Environment with Modular Structure (POEM), developed at Institute of Aerodynamics and Gasdynamics [26]. This tool consists of three main modules, namely the optimizer module, the geometry module, and the analysis module. Several flow solvers like MSES and XFOIL are available for two-dimensional flows, whereas three-dimensional flows are evaluated using the FLOWer code. The optimization algorithm applied in this work was a Downhill–Simplex optimizer. A set of design variables was passed from the optimizer to the geometry module which generated the appropriate geometrical model for the design. Evaluation of this design was then performed using the FLOWer code that returned the corresponding objective function value to the optimizer. An automatic script-based grid generation method was used to produce the required finite volume grids for the modified airfoil geometries.

B. Modeling of the Wind Tunnel

Simulation of the wind-tunnel walls was motivated by systematic discrepancies between the experimental results and the CFD simulations conducted beforehand using far-field boundary conditions. Preliminary studies using two-dimensional models were conducted to specify the detail level of the modeling necessary to capture the relevant wall interference effects in the wind tunnel. Simulation of the two-dimensional airfoil and the wind-tunnel test section, with the upper and lower walls modeled, showed the tendency of improving the agreement between numerical and experimental results. However, the presence of the upper and lower wind-tunnel walls did not explain all of the differences between measurements and numerical freestream simulations. Additional influences from the test section's side walls required the three-dimensional modeling of the complete test section.

Furthermore, the preliminary studies showed a noticeable influence of the thickness and condition of the wall boundary layer on the overall flow condition in the test section in general and on the shock wave/boundary-layer interaction in particular. The influence on the overall flow in the channel was due to the displacement effect of the boundary layer which reduced the effective flow cross section. However, no information on the displacement thickness of the boundary layer at the conditions tested was available from the measurements to be prescribed at the simulation's inflow section. A realistic boundary-layer history was therefore provided at the test section entry by additional modeling of the nozzle and the settling chamber ahead of the test section, following the work of Melber-Wilkending et al. [27] regarding the DNW-NWB low-speed wind tunnel in Braunschweig, Germany. The flow straightener upstream of the settling chamber in the wind tunnel effectively removed the boundary layer and, thus, a new boundary layer developed, beginning from the settling chamber entry plane. Starting the numerical simulation with the flow in the settling chamber offered the possibility of simulating the boundary-layer development through the nozzle and into the test section as realistically as possible.

Figure 2 illustrates the numerical model of the wind tunnel with the airfoil model mounted into the test section. The contour of the adaptive walls test section was modeled individually for each flow condition based on the measurement data. The positions of the upper and lower adaptive walls, which were recorded at the TWG for each flow condition, were applied to the baseline geometry of the test section. An additional correction of the wall position in the rear part of the test section was introduced as a simple way to account for the displacement effect of the wake rake rather than modeling the rake itself.

Figure 3 shows a comparison of the measured pressure distribution along the test section center plane to the numerical results. Two CFD solutions illustrate the influence of the wake rake displacement and the effect of the aforementioned displacement correction.

All of the walls of the wind tunnel and the airfoil model surface were modeled with no-slip wall boundary conditions. A symmetry plane was specified along the wind-tunnel center to reduce the computational costs. Inflow to the settling chamber and outflow of the test section were modeled using special inflow and outflow boundary conditions. These boundary conditions made use of two versions of the characteristic theory specialized to subsonic inflow and outflow. At the inflow plane, the total pressure p_0 and the total temperature T_0 were specified for each flow condition separately according to the recorded values from the measurements. The total values p_0 and T_0 in the simulation corresponded to the fluid state in the reservoir, which equals the ambient pressure and temperature in the case of this campaign. Flow velocity in the numerical wind tunnel

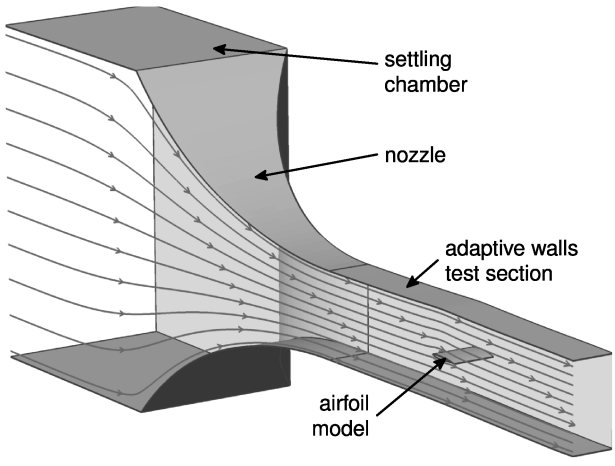

Fig. 2 CFD half-model of the adaptive walls test section of the TWG with nozzle and settling chamber.

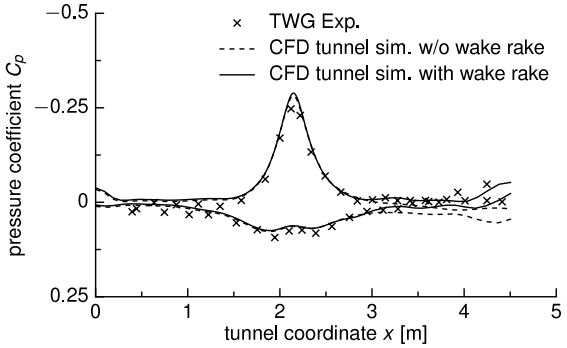

Fig. 3 Pressure distribution in the wind-tunnel center plane.

was adjusted by specifying the static pressure p_{exit} at the outflow plane. The FLOWer code offers an automatic routine to iteratively adjust p_{exit} until a target flow speed is achieved at a prescribed position in the flow domain. However, for most of the simulations, the outflow static pressure was set based on measured values from the most downstream pressure orifices in the test section, to avoid the time consuming iteration process of p_{exit}. Comparisons between both methods of setting the exit pressure were performed at selected angles of attack and it was found that a similar accuracy could be achieved.

Block-structured finite volume grids were generated automatically and individually for each flow condition based on the respective contours of the adaptive walls and the airfoil's angle of attack. A study on different sized grids was conducted to determine the grid resolution necessary to capture all relevant flow effects. Three grids with a refinement ratio of approximately 1.5 in each index direction were produced leading to overall numbers of grid cells of 5.6×10^6, 18.8×10^6, and 68.3×10^6 for the coarse, medium, and fine grid, respectively. Figure 4 shows the drag coefficient versus a grid size index for the three different grid sizes. The grid size index is defined as the number of grid cells N raised to the $-\frac{2}{3}$ power to give the square of a representative average cell size. For second-order accurate discretization schemes like the FLOWer code employed, the results should produce a straight line [28]. Additionally, Fig. 5 shows an

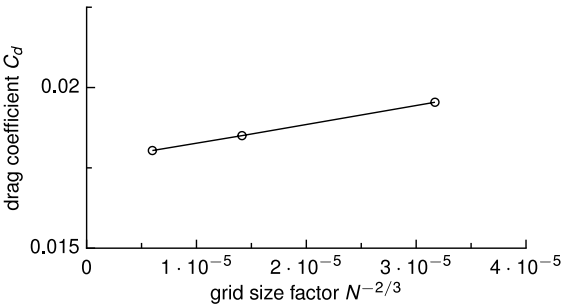

Fig. 4 Drag coefficient versus grid resolution index for grid refinement study on three grids.

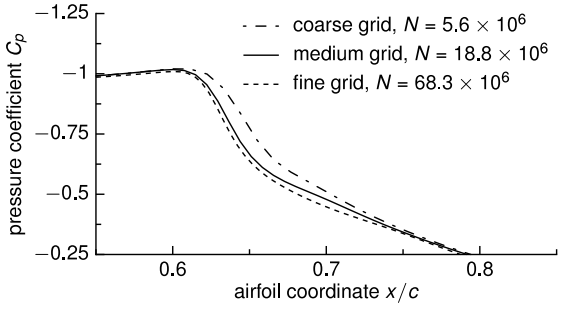

Fig. 5 Influence of grid resolution on shock location.

influence of the grid resolution on the shock location on the baseline airfoil but with only small differences between the medium and the fine grids. Based on the results of the grid refinement study, a final regular grid was set up based on the medium-sized grid but with a slightly higher resolution on the airfoil surface. A total of 384×256 cells were placed on the half-span of the airfoil model in the streamwise and spanwise direction, respectively. The SCBs close to the symmetry plane were reproduced using 24×32 cells on their surface, with a tight normal grid spacing of $y^+ \leq 0.5$ to ensure correct resolution of the shock/boundary-layer interactions. Wall spacing was specified such that $y^+ \leq 1$ in the inflow and the middle of the test section and $y^+ \leq 2$ in the outflow region. The overall size of the final grid for the half-model was 22×10^6 cells.

IV. Design of Three-Dimensional Shock Control Bumps for Wind-Tunnel Testing

A. Design for Testing

The contour of the shock control bumps tested in the TWG was specifically designed for the test campaign. Its development was driven by the requirements for a good aerodynamic performance as well as a high robustness of the design. The high robustness was deemed necessary, as it was expected from the beginning that the wind tunnel would somewhat influence the shock position compared to the CFD simulations and thereby deteriorate the SCB performance.

The design point was chosen so that the airfoil operated at off-design condition in the drag-rise region. A prerequisite for the design point was the occurrence of shock waves with a certain shock strength but without significant shock-induced separation. A range of inflow conditions was examined using MSES and the flow condition for the design point was chosen as follows: $M = 0.79, Re = 5 \times 10^6$, $C_l = 0.75$, and $L/D = 43.6$. The MSES calculation showed a contribution of the wave drag of about 30% of the total drag for the given airfoil. The design lift coefficient of $C_l = 0.75$ was reached at an angle of attack of $\alpha = 1.85$ deg using the FLOWer code.

The base shape of the bumps, as will be explained in detail in Sec. IV.B, was selected as a good compromise between performance and robustness. This shape is characterized by a ratio of width/length $\lessapprox 1$ and discontinuities at the slopes of the upstream and the sideward flanks. The rear flank blends continuously in the airfoils suction side. The contour is based on the elastic deflection lines of bending beams as shown in Fig. 6a. Thorough investigations on various discretizations of shock control bumps, including the flexible beam method used herein, can be found in Sommerer [7] and Pätzold [15].

The width of the bump design was constrained to 10% chord length or 4 cm because of the limitations due to the stationary-mounted wake rake and therefore the limited spanwise extent of stations for drag measurements. The distance between two consecutive bumps was set to 10% chord length as well, whereas the bump length was fixed to $l_{\text{scb}} = 20\%$. Direct numerical optimization using the POEM tool was applied to the limited set of two remaining design parameters: the position of the bump crest x_{pos} and the height of the crest h_{scb}. The crest position also corresponds to the center point of the bump.

Table 2 gives the optimized parameters and the gain in aerodynamic efficiency as well as a modified set of optimized parameters with a slightly reduced height for improved robustness. Figure 6b shows an isometric view of the final SCB design. A detailed description of the design of the three-dimensional shock control bumps for wind-tunnel testing at TWG is given in [15].

B. Three-Dimensional Shock Control Bumps: Physical Mechanisms

The classic contour bump, as it was first described by Ashill et al. [5], works by inducing isentropic recompression waves from its smooth concave upstream flank. A novel bump design that features a kink at the foot of its upstream flank rather than a smooth transition was described by the University of Cambridge [10,11,16] and further investigated by Pätzold [15]. This bump design uses a bifurcated

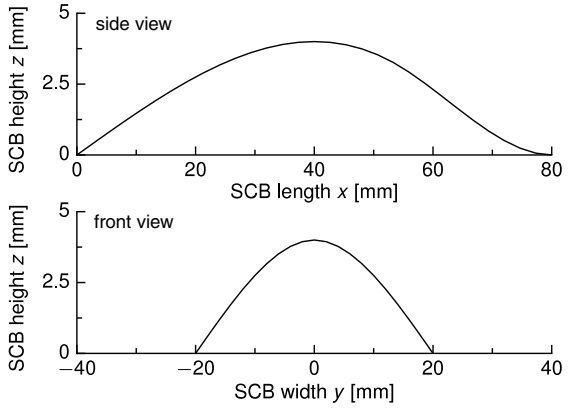

a) Front and side view of the bump contour

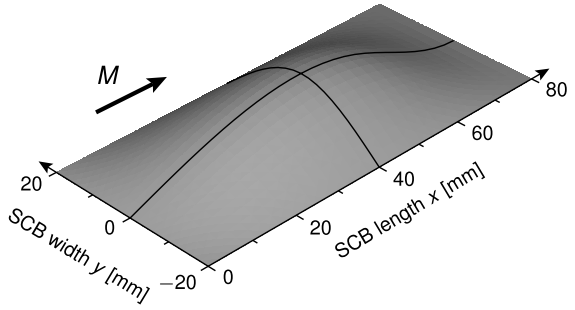

b) Isometric view of the bump

Fig. 6 Three-dimensional shock control bump design.

shock structure, a so-called λ shock, instead of the isentropic recompression waves. The series of oblique shocks of the λ shock realizes the same pressure jump as the original normal shock with reduced total pressure losses. Whereas the classic bump design offers slightly higher drag reductions, the new design benefits from an improved robustness against variations in the shock location. Pätzold showed that this is because of the front shock leg of the λ shock being fixed in position at the kink of the bump's upstream flank. This prevents excessive flow acceleration across the bump in case of a misalignment of the bump and the shock. The new bump contour concept is applicable both to two- and three-dimensional bump shapes.

Figure 7 shows contour plots of the Mach-number distribution in a cutout of the shock region on the suction side for the baseline airfoil and the airfoil with the optimized three-dimensional bump contour from Sec. IV.A. Whereas the baseline airfoil exhibits a strong normal shock wave, the SCB-induced λ structure of the shock is clearly visible for the airfoil with bump.

Three-dimensional shock control bumps, as they have been investigated in this work, have small width/length ratios. Therefore, the flow across such a bump is inherently three-dimensional and this gives rise to additional effects that do not occur in the case of two-dimensional bumps with high width/length ratios. The main effect is the spanwise influence of the bump-induced compression waves, well beyond its actual span. The region of influence is described by the three-dimensional characteristics running out of the local disturbances of the supersonic flow by the bump. Given a well-chosen spacing of an array of 3D-SCBs, the individual regions of influence can overlap such that the resulting shock structure is fairly

Table 2 Optimized SCB parameters and parameters for increased robustness

	x_{pos}	h_{scb}	ΔC_l	ΔC_d	$\Delta L/D$
Optimized design	$0.728c$	$0.0155c$	−1.10%	−9.13%	+8.85%
Modified design	$0.729c$	$0.0100c$	−0.32%	−6.63%	+6.74%

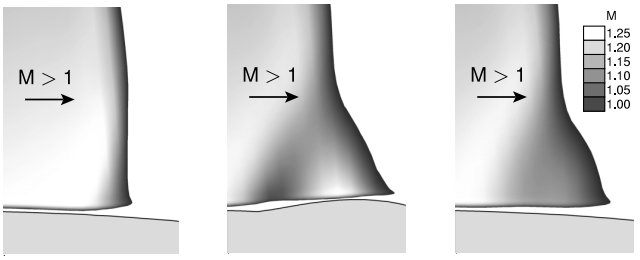

a) Baseline airfoil b) SCB center plane c) Between SCBs

Fig. 7 Mach contours of the baseline airfoil and with 3D-SCB at two spanwise positions.

two-dimensional. This can be seen by a comparison of Figs. 7b and 7c, showing the center plane of the bump and a plane midway between two consecutive bumps, respectively. The front shock leg in between the bumps is located slightly downstream of the one in the center plane, corresponding to the downstream component of the characteristics, but the overall λ shock has a roughly two-dimensional structure.

The pressure distribution in the shock region is depicted in Fig. 8, again for the baseline airfoil and two positions at the center of an SCB and midway in between. The pressure jump across the normal shock on the clean airfoil is replaced by the pressure signature of the λ shock in the center plane of the bump. At first glance, this surface pressure distribution across the bump center does not seem to be favorable. It rather indicates a strong deceleration that could be taken for a normal shock wave with a following reacceleration of the flow to approximately the same minimum pressure level as in the clean case. However, Fig. 7b shows that these strong pressure, and thereby flow velocity, variations are limited to a small region right above the bump surface. In fact, the first pressure rise corresponds to the front leg of the λ shock. The very strong reacceleration is caused by the considerable height of the bump of 1.5% of the chord length in this particular case, but it must be pointed out that this effect is locally limited to the immediate vicinity of the bump crest. Farther away from the bump's surface, the Mach-number contours indicate a much more beneficial velocity profile, as does the surface pressure distribution midway between the SCBs. This can also be seen in Fig. 9, where the loss in total pressure, due to the shock, is illustrated at the trailing edge. The total pressure losses, due to the boundary layer, are hidden in this illustration for the sake of clarity. Despite the seemingly unfavorable surface pressure distribution across the bump, there is a distinct reduction of the total pressure loss caused by the shock along the span. This reduction is again fairly two-dimensional with only very weak three-dimensional structures.

One particular effect that is due to the strong surface pressure variations across the bump is depicted in Fig. 10. The adverse pressure gradient behind the bump crest and the spanwise pressure gradients at the sideward flanks create a pair of counter-rotating vortices at the rear surface of the bump. The velocities induced by this

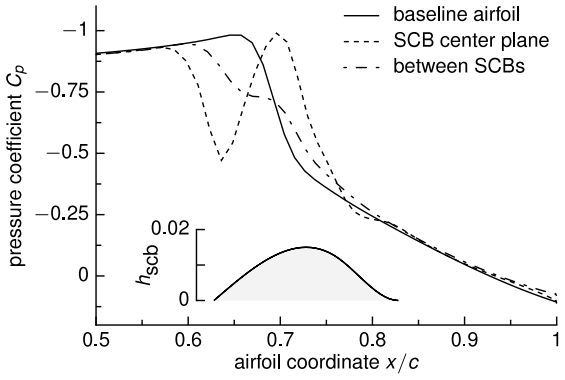

Fig. 8 Surface pressure distributions at the shock position.

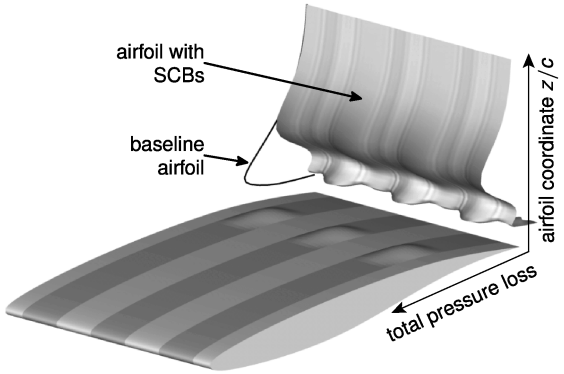

Fig. 9 Spanwise distribution of the total pressure loss; baseline given for comparison.

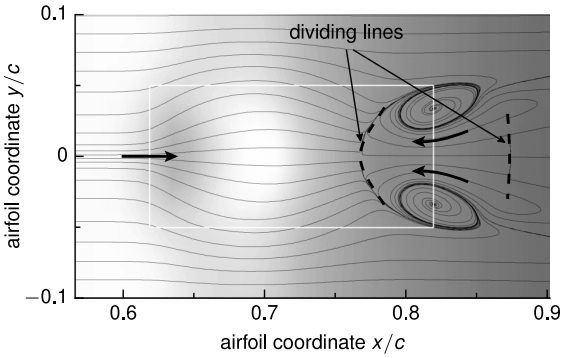

Fig. 10 Surface pressure distribution and streamlines in the bump region.

vortex pair form a local recirculation area at the downstream side of the bump. The displacement thickness shown in Fig. 11 grows rapidly in this region but the effect is limited locally. Toward the trailing edge, the displacement thickness in a plane parallel to the freestream velocity is even smaller behind the bump than midway between two bumps. Even though this is subject to further research, it seems to indicate a stabilizing effect of the vortices on the boundary layer downstream of the bump. It may also be reasoned that these vortices have a contrary effect on the boundary layer between the bumps, which could explain its increased thickening toward the trailing edge shown in Fig. 11.

The three-dimensional character of the bumps leads, in general, to variations of local lift distribution with the consequence of an additional induced-drag component. The aforementioned vortical structures may counteract this effect. A detailed study of these mechanisms is given in [15]. The optimizations presented in Sec. IV.A took these effects and the potential additional induced drag into account by considering the integral aerodynamic efficiency of the design.

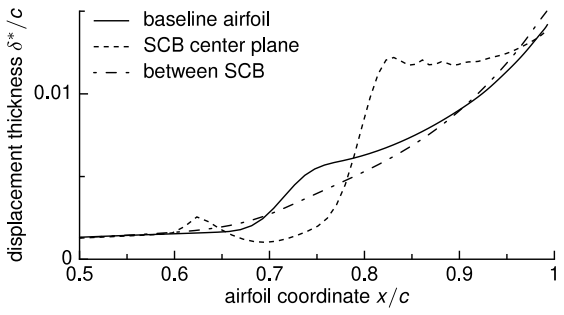

Fig. 11 Comparison of the displacement thickness in the shock region.

V. Results

A. Experimental Results

A numerical and experimental assessment of the 3D-SCB design introduced in Sec. IV.A was conducted in the TWG. The experimental results obtained showed significant drag reductions for $\alpha > 1.9$ deg. A drag reduction of approximately 10% was achieved for a wide range of angles of attack in the drag-rise region of the baseline airfoil. Figure 12 shows drag polars obtained by numerical simulation and from measurements in the TWG at $M = 0.79$ and $Re = 5 \times 10^6$, whereas Fig. 13 illustrates the relative drag reductions. Because of the aforementioned tight time schedule, tests were only performed for the design Mach number of $M = 0.79$ rather than for a range of Mach numbers. Therefore, only C_d-α polars are available but no M-α polars. To obtain the overall drag from the measurements at the five spanwise positions, a smoothing function was integrated between the local drag measurements $dY = 0$ to 40 mm. The CFD simulations depicted in Figs. 12 and 13 were performed using the same SCB design tested in the TWG but freestream boundary conditions, instead of wind-tunnel walls, were applied.

The experimental and the numerical results showed similar behavior in the drag-rise region of the polars, and, in particular, the drag reductions of the same size were achieved. However, there were considerable discrepancies regarding the onset of the drag rise and the deterioration of aerodynamic efficiency, due to the bumps at small angles of attack, and the minimum drag of the baseline airfoil. These discrepancies could be attributed to residual wall interferences present in the wind tunnel despite the wall adaptation that was performed. These effects will be analyzed in the following section.

B. Wall Interference Effects

Despite the application of the TWG's adaptive walls test section, the experimental results showed clear indication for the presence of residual wall interference effects at this high Mach number. Similar

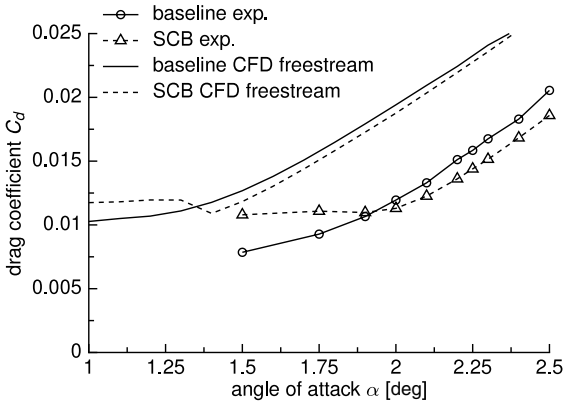

Fig. 12 Comparison of measured and computed drag.

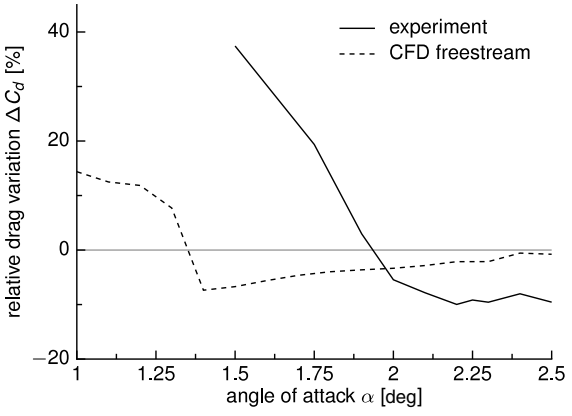

Fig. 13 Relative drag reduction due to the SCB.

findings had been previously reported by Milholen and Owens [29] for NASA Langley's 0.3 m Transonic Cryogenic Tunnel. To include the interference effects into the numerical analysis, the wind tunnel was modeled and implemented into the simulations as described in Sec. III.B. The simulations showed that the main characteristic of the interferences are shock waves originating from the junction of the model's leading edge and wind-tunnel side walls, propagating in the spanwise direction through the supersonic flow area on the airfoil's suction side. The propagation angle of these oblique shock waves depends on the local Mach number. Additional information on the structure of the two- and three-dimensional interferences were presented by König et al. in [18].

The deceleration of the supersonic flow across these oblique shocks upstream of the main shock leads to lower wave drag in the wind tunnel compared to the freestream simulations. This results in the delayed onset of the drag rise shown in Fig. 12. At specific onflow conditions at small angles of attack, the interference shock waves provide the main pressure recovery and remove the weak shock usually existing in the airfoil flow without wall interferences. This effect can clearly be seen in Fig. 14 and, as a result, the subsonic drag level is reached earlier. The illustration shows the shock position on the clean airfoil's suction side in the experiment and in the simulations with and without wind-tunnel walls. A distinct shock developed in the freestream simulations already at $\alpha = 1.0$ deg, whereas both the measurements and the simulations with wind-tunnel walls showed a delayed formation of a shock starting at higher angles of attack. The principle effect of this delayed development of a shock is captured very well in the wind-tunnel CFD simulations, even though there is a small discrepancy in the first occurrence of a weak normal shock at $\alpha \approx 1.5$ deg compared to $\alpha \approx 1.75$ deg in the experiment.

The good agreement of the numerical wind-tunnel simulations and the experiment can also be seen in Fig. 15. It shows the relative drag reductions due to the bumps versus the angle of attack for the CFD computation with and without accounting for the wind-tunnel walls compared with the measurements. The simulation with walls reproduced the model's behavior in the wind tunnel very well in a range of small to medium angles of attack.

In particular, the very high drag penalty of about 40% at $\alpha = 1.5$ deg is very well reflected in the simulation. Here, the flow conditions of the baseline airfoil at $\alpha = 1.5$ deg are such that the side wall interferences neutralize the main shock and thereby lead to a local reduction of C_d compared with the freestream, which can also be clearly seen in Fig. 12. The application of the shock control bump at these conditions results in a strong reacceleration of the flow, which finally leads to a bump-induced normal shock with considerable additional wave drag. Figure 16 shows pressure distributions obtained by PSP at $\alpha = 1.5$ deg in the bump's center plane and in between two consecutive bumps. The shock induced by the bump is clearly visible. The shock-free C_p distribution of the baseline airfoil, measured by means of conventional pressure taps, is given for comparison.

The discrepancy between the wind-tunnel simulation and the measurements seen in Fig. 15 at $\alpha = 1.75$ deg (with the simulation showing a drag reduction, whereas the measurements yielded a substantial drag penalty) can also be explained by an additional bump-induced normal shock in the experiment. For this airfoil, the shock location is highly sensitive to the flow conditions just upstream of the shock. Very small inaccuracies in the simulation may thereby lead to considerable variations in the shock position and strength. Hence, the simulation already shows a normal shock at a position close to the bump and the associated wave drag is reduced by the shock control bump. The very weak shock in the experiment at $\alpha = 1.75$ deg has no significant wave drag yet, and it is also located too far upstream of the bump. Thus, the SCB induces a normal shock with considerable wave drag.

For $\alpha > 1.75$ deg, the agreement between the measurements and the numerical simulations is very good, which is also exemplarily shown in Fig. 17 for the baseline airfoil at a flow condition of $M = 0.79$ and $\alpha = 2.25$ deg. The CFD simulation with freestream

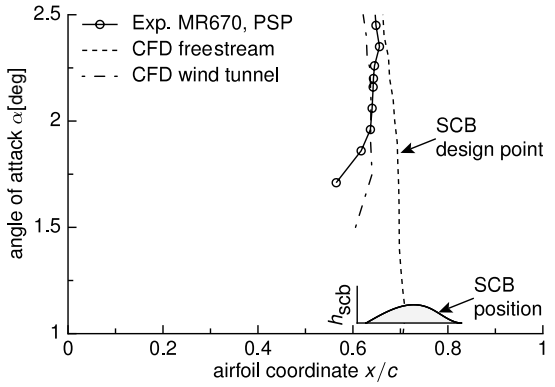

Fig. 14 Shock position on the clean airfoil for varying angle of attack.

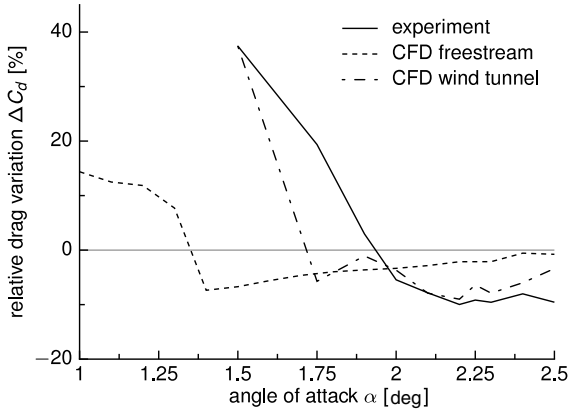

Fig. 15 Comparison of the impact of the wind-tunnel walls on the relative drag reduction.

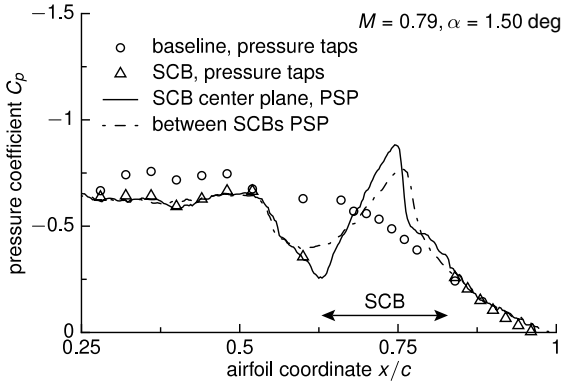

Fig. 16 Measured C_p distribution with bump-induced shock (conventional pressure taps and PSP).

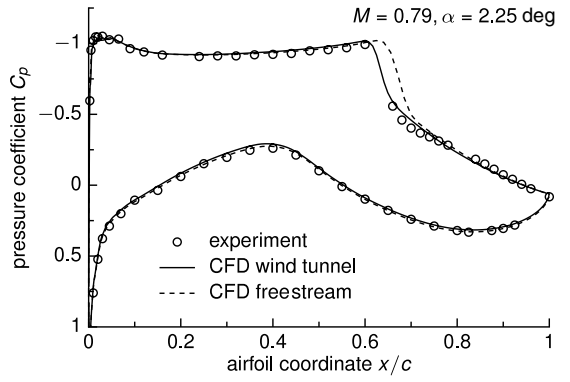

Fig. 17 Pressure distributions of the baseline airfoil; simulations with freestream conditions and with wind-tunnel environment.

boundary conditions yielded a downstream offset of the shock location of about 5% of the chord length compared with the measurements, whereas modeling of the wind-tunnel environment in the CFD simulations captured the shock location in very good agreement with the experimental results.

As shown in Fig. 14, the wall impact caused a general shift in the shock position of no less than 5% of the chord length compared to the freestream conditions assumed in the SCB design. For wind-tunnel conditions, the bumps were actually located too far downstream and the SCBs were operating at off-design conditions. Nevertheless, a drag reduction of about 10% could be achieved in the drag rise, even though the intended physical SCB mechanisms were affected by the wall interferences.

VI. Conclusions

A novel type of three-dimensional shock control bump was investigated numerically and experimentally at the Transonic Wind Tunnel Göttingen. The purpose of these experiments was the validation, both of the new 3D-SCB concept and of the numerical CFD method used for the design and analysis. The drag reductions found in the experiment were of the same size as predicted numerically but the results were affected by wind-tunnel interference effects. These wall interferences resulted in a shift of the shock location and the SCBs were therefore operated at off-design conditions. By careful modeling of the wind-tunnel environment in the numerical simulations, the wall impact on the flow could be reproduced in quality and quantity. Good agreement was achieved between the experimental results and the numerical simulations of the wind-tunnel environment.

Acknowledgments

This work has partly been funded by Deutsche Forschungsgemeinschaft. The authors would like to express their gratitude to the teams of the Transonic Wind Tunnel Göttingen and DLR, German Aerospace Center for supporting the tests. Discussions with S. Melber-Wilkending from DLR, German Aerospace Center provided helpful insights into the numerical simulation of wind-tunnel environments.

References

[1] Schneider, W., "The Importance of Aerodynamics in the Development of Commercially Successful Transport Aircraft," *Aerodynamic Drag Reduction Technologies*, edited by P. Thiede, Vol. 76, Notes on Numerical Fluid Dynamics, Springer, New York, 2000, pp. 9–16.

[2] Stanewsky, E., Delery, J., Fulker, J., and de Matteis, P. (eds.), *EUROSHOCK II: Drag Reduction by Shock Boundary Layer Control. Notes on Numerical Fluid Mechanics and Multidisciplinary Design*, Vol. 80, Springer-Verlag, New York, 2002.

[3] Knauer, A., "Performance Improvement of Transonic Airfoils Through Contour Modifications in the Shock Region," DLR, German Aerospace Center Research Rept. 98-03, 1998; also Ph.D. Thesis, Universität Hannover, Hannover, Germany, 1998.

[4] Birkemeyer, J., "Drag Minimization on a Transonic Wing by Ventilation and Adaptive Contour Bumps," DLR, German Aerospace Center Research Rept. 1999-28, 1999; also Ph.D. Thesis, Universität Hannover, Hannover, Germany, 1999.

[5] Ashill, P. R., Fulker, J. L., and Shires, A., "A Novel Technique for Controlling Shock Strength of Laminar-Flow Aerofoil Sections," Deutsche Gesellschaft für Luft- und Raumfarht Paper 92-01-022, March 1992.

[6] Sommerer, A., Lutz, T., and Wagner, S., "Design of Adaptive Transonic Airfoils by Means of Numerical Optimisation," European Congress on Computational Methods in Applied Sciences and Engineering Paper ECCOMAS2000-253Sept. 2000.

[7] Sommerer, A., "Numerische Optimierung Adaptiver Transsonischer Profile," Ph.D. Thesis, Inst. für Aerodynamik und Gasdynamik, Univ. Stuttgart, Stuttgart, Germany, 2005.

[8] Kutzbach, M., Lutz, T., and Wagner, S., "Investigations on Shock Control Bumps for Infinite Swept Wings," AIAA Paper 2004-2702, 2004.

[9] Rosemann, H., Richter, K., Birkemeyer, J., Rodde, A.-M., and Schmitt, V., "Application of a 3-D Shock Control Bump on a Transport Aircraft Configuration," ONERA/DLR Paper S1-4, June 2003.

[10] Holden, H. A., and Babinsky, H., "Shock/Boundary Layer Interaction Using 3D Devices," AIAA Paper 2003-447, Jan. 2003.

[11] Babinsky, H., and Ogawa, H., "Three-Dimensional SBLI Control for Transonic Airfoils," AIAA Paper 2006-3698, June 2006.

[12] Rein, M., Rosemann, H., and Schülein, E., "Wave Drag Reduction by Means of Aerospikes on Transonic Wings," *Shock Waves: 26th International Symposium on Shock Waves*, Vol. 2, Springer, Berlin, 2009, pp. 1309–1313.

[13] Qin, N., Wong, W., Moigne, A. L., and Sellars, N., "Validation and Optimisation of 3D Bumps for Transonic Wing Drag Reduction," Confederation of European Aerospace Societies Paper CEAS/KATnet-36, June 2005.

[14] Pätzold, M., Lutz, T., Krämer, E., and Wagner, S., "Numerical Optimization of Finite Shock Control Bumps," AIAA Paper 2006-1054, Jan. 2006.

[15] Pätzold, M., "Auslegungsstudien von 3-D Shock-Control-Bumps mittels numerischer Optimierung," Ph.D. Thesis, Inst. für Aerodynamik und Gasdynamik, Univ. Stuttgart, Stuttgart, Germany, 2009.

[16] Ogawa, H., Babinsky, H., Pätzold, M., and Lutz, T., "Shock/Boundary-Layer Interaction Control Using Three-Dimensional Bumps for Transonic Wings," *AIAA Journal*, Vol. 46, No. 6, June 2008, pp. 1442–1452.
doi:10.2514/1.32049

[17] Holst, H., and Bock, K.-W., "Wall Adaptation and Determination of Residual Wall Interferences for a 2D and a 3D Model in the Transonic Wind Tunnel TWG of DLR," *International Congress on Instrumentation in Aerospace Simulation Facilities*, Inst. of Electrical and Electronics Engineers, New York, 1997, pp. 174–184.
doi:10.1109/ICIASF.1997.644679

[18] König, B., Lutz, T., and Krämer, E., "Numerical Simulation of a Transonic Wind Tunnel Experiment," *High Performance Computing in Science and Engineering '08*, edited by W. Nagel, D. Kröner, and M. Resch, Springer-Verlag, Berlin, 2008, pp. 381–393.

[19] Amecke, J., "Direct Calculation of Wall Interferences and Wall Adaptation for Two-Dimensional Flow in Wind Tunnels with Closed Walls," DFVLR Tech. Rept. DFVLR-FB 85-62, Göttingen, Germany, 1985 (published in German).

[20] Klein, C., Engler, R., Sachs, W., and Henne, U., "Application of Pressure Sensitive Paint (PSP) for Determination of the Pressure Field and Calculation of Forces and Moments of Models in a Wind Tunnel," *Experiments in Fluids*, Vol. 39, No. 2, 2005, pp. 475–483.
doi:10.1007/s00348-005-1010-8

[21] Sobieczky, H., "DLR-F5: Test Wing for CFD and Applied Aerodynamics," *AGARD R303-A Selection of Experimental Test Cases for the Validation of CFD Codes*, Vol. 2, AGARD Advisory Rept. 303, 1994, pp. 253–263.

[22] Giles, M. B., and Drela, M., "Two-Dimensional Transonic Aerodynamic Design Method," *AIAA Journal*, Vol. 25, No. 9, Sept. 1987, pp. 1199–1206.
doi:10.2514/3.9768

[23] Fassbender, J. K., and Kroll, N. (eds.), MEGAFLOW-Numerical Flow Simulation for Aircraft Design: Results of the Second Phase of the German CFD Initiative MEGAFLOW, Vol. 89, *Notes on Numerical Fluid Mechanics and Multidisciplinary Design (NNFM)*, Springer, New York, Dec. 2005, ISBN 9783540323822.

[24] Swanson, R. C., and Turkel, E., "On central-difference and upwind schemes," *Journal of Computational Physics*, Vol. 101, No. 2, 1992, pp. 292–306.
doi:10.1016/0021-9991(92)90007-L

[25] Wilcox, D. C., *Turbulence Modeling for CFD*, 3rd ed., DCW Industries, La Cañada, CA, 2006, ISBN 1-928729-08-8

[26] Lutz, T., Sommerer, A., and Wagner, S., "Parallel Numerical Optimisation of Adaptive Transonic Airfoils," *Fluid Mechanics and its Applications*, Vol. 73, Kluwer Academic, Norwell, MA, 2003.

[27] Melber-Wilkending, S., Heidebrecht, A., and Wichmann, G., "CFD Validation by Wind Tunnel Measurements: Uncertainty Assessment by Numerical Simulation of Complete Wind Tunnel Flows," *NATO-RTO, Applied Vehicle Technology, AVT 147*, 2007.

[28] Lee-Rausch, E. M., Buning, P. G., Morrison, J. H., Park, M. A., Rivers, S. M., Rumsey, C. L., and Mavriplis, D., "CFD Sensitivity Analysis of a Drag Prediction Workshop Wing/Body Transport Configuration," *21st AIAA Applied Aerodynamics Conference*, AIAA Paper 2003-3400, June 2003.

[29] Milholen, W. E., and Owens, L. R., "On the Application of Contour Bumps for Transonic Drag Reduction (Invited)," *43rd AIAA Aerospace Sciences Meeting and Exhibit*, AIAA Paper 2005-0462, Jan. 2005.